Title

Synthetic lipid rafts formed by cholesterol nano-patch induce T cell activation

Authors

Yunmin Jung [1], Young-Joo Kim [1,2], Sunmi Lee [1], Jungmin Nam [1,2], Seonyeong Ha [1,2], Jinwoo Cheon [1,2,3,*], Minsuk Kwak [1,2,*]

Affiliations

[1] Institute for Basic Science Center for Nanomedicine, Seoul 03722, South Korea

[2] Department of Nano-Biomedical Engineering, Advanced Science Institute, Yonsei University, Seoul 03722, South Korea

[3] Department of Chemistry, Yonsei University, Seoul 03722, South Korea

*e-mail: minsuk.kwak@yonsei.ac.kr, jcheon@yonsei.ac.kr

Abstract

Lipid rafts are small and dynamic membrane compartments that are enriched with cholesterols or sphingolipids. The coalescence of small lipid rafts into a large lipid raft forms a signaling platform at the immunological synapse that plays a crucial role in controlling T cell activation. Cholesterol is a major component for the formation and function of lipid rafts, but the relationship between the spatial configuration of cholesterols and the lipid raft mediated membrane segregation as well as TCR signaling remains poorly understood. Here we used cholesterol conjugated DNA origami nanostructures, cholesterol nano-patch (CNP) to construct lipid rafts on intact live T cells. CNPs are two-dimensional DNA scaffolds that allow controlling the spatial presentation of cholesterols in the plasma membrane. CNPs efficiently bind onto the T cell membrane and rapidly induce large, polarized membrane cap structures which colocalize with flotillin-1. These CNP mediated membrane segregations, which we define as synthetic lipid rafts, drive membrane segregation of key signaling molecules including TCR and CD45, thereby triggering downstream TCR signaling and subsequently functional T cell responses without antigenic challenges. Our work highlights the potential of CNP in uncovering the mechanisms that lipid rafts induced by cholesterols drive membrane protein reorganization and control T cell signaling, and offers valuable insights into the design of antigen-independent immunotherapies.

Keywords

Lipid rafts, Synthetic lipid raft, Cholesterol, Cholesterol nano-patch, T cell activation, CD45 exclusion, DNA origami, TCR accumulation, Flotillin, Polarization.

Introduction

Lipid rafts are specialized membrane compartments containing high cholesterol or sphingolipids [1,2]. Due to their more ordered, thicker, and less fluidic characteristics, lipid rafts contribute to the spatial organization of membrane proteins and influence abroad arrays of cellular signaling events [3-6]. Lipid rafts are nanoscale assemblies (10–200 nm) that can be stabilized to form a large platform for controlling cell signaling [1,3]. Cholesterol is an essential component of the lipid raft and is involved in a large variety of cellular functions [7-11]. In synthetic model membranes or in molecular simulations, high contents of cholesterol can drive spontaneous liquid-liquid phase separation (LLPS) of the lipids in the membrane, and the concentration of cholesterols showed a high correlation with the formation of liquid-ordered (Lo) phase lipid domain [12-15]. It is also known that cholesterols form a thicker lipid bilayer therefore it influences the positioning of the membrane proteins [16-18].

In T cells, a large coalescence of lipid rafts is formed at the immunological synapses between T cells and APCs and serve as the signaling platform for T cell activation by driving spatial reorganization of key signaling molecules [19-22]. T cell receptors (TCR) and other signaling molecules, such as Lck, LAT, or ZAP70 are recruited into the large lipid raft at IS, while phosphatase CD45 is excluded from it [6,23,24]. The role of cholesterol in T cells has been studied by enrichment using squalene administration or inhibiting cholesterol esterification, or by extraction with methyl-β-cyclodextrin in the whole cell membrane showing that modulation of cholesterol homeostasis profoundly influences T cell functions [25-28]. There are two opposing effects of cholesterol in regulating TCR at the molecular level has been suggested [29] that binding of cholesterol to TCR stabilizes its inactive conformation [30,31] or binding of cholesterol causes TCR nanoclustering which enhances the avidity of the TCR-antigen interaction and positively regulates T cell activation [9]. Another recent study suggested that cholesterol regulates CD45 exclusion at the tip of microvilli in T cells at their resting state [17]. However, due to the technical limitation for controlling the distribution or density of cholesterols in the live cell membrane, how the spatial organization of cholesterols modulates lipid-raft-driven protein segregation and downstream TCR signaling is largely unknown.

To directly investigate the roles of cholesterols in the coalescence of lipid rafts formation and protein partitioning in T cells, we designed a DNA origami nanostructure, cholesterol nano-patch (CNP) as a nanosized lipid raft-like monomer when it attaches to the membrane. On a single CNP, we can organize multiple cholesterols in a programmable manner to artificially induce lipid rafts by creating a high local density of cholesterols on the cell membrane. The controllable architecture of DNA origami has been applied to manipulate the spatial configuration of biomolecules with nanoscale precision [32,33] . Our result showed that the CNP binds to the outer leaflet of the T cell membrane and forms a large and stably polarized cluster. We defined this large coalescence of multiple CNPs segregated into a distinctive domain via

enrichment of cholesterols as a synthetic lipid raft. This CNP-mediated synthetic lipid raft co-polarized with lipid raft protein flotillin-1 [34]. We found that CD45 molecules are largely excluded from the synthetic lipid rafts, supporting the lipid raft mediated CD45 exclusion mechanism. Furthermore, the formation of the synthetic lipid raft drives TCR accumulation to it and enhances CD69 expression and ZAP-70 phosphorylation. These results illustrate that the local concentration of cholesterols drives the formation of large, polarized lipid rafts on T cell membranes that induce the spatial reorganization of signaling molecules, activating T cells independent of antigenic challenges. Our results demonstrate the capability of DNA origami in interrogating the mechanism of lipid raft-driven protein segregation on T cell membrane and reveal the role of nanoscale arrangement and local concentration of cholesterols in regulating T cell signaling.

Results

Design of DNA origami structure for cholesterol patterning.

We fabricated sheet-like DNA nanostructures, DNA nano-patch (NP), employing a DNA origami method to construct a molecular template where the number or arrangement of cholesterols can be programmed. (Fig. 1). DNA origami is a molecular fabrication technique enabling the construction of a customized nanostructure with desired shape and size [32,33]. By folding a long single-stranded DNA (ssDNA) into a target geometry through rationally designed hybridizations with multiple short ssDNAs, a customized DNA nanostructure can be easily constructed with high shape accuracy. The DNA NP is a square sheet with a side of 60 nm and a height of 6 nm (**Fig. 1a, b and Supplementary Table. 1**). To control the number of cholesterols on it, an array of anchors was designed on one side, where additional ssDNA (DNA handles) can be extended to accommodate cholesterol-conjugated DNAs (Chol-DNAs). Each DNA NP can display up to 72 Chol-DNAs in an array of 12 x 6 with rows and columns separated by 3.5 nm and 7 nm, respectively, which enables inter-cholesterol spacing from up to 3.5 nm to 38.5 nm (**Fig. 1a**). The DNA NP also contains Cy5-fluorophores at each of four corners to allow for visualization. Through hybridization of DNA handles with Chol-DNA strands and assist DNAs, which formed a stable duplex with Chol-DNA, a DNA NP is converted to a cholesterol nano-patch (CNP), which facilitates the hydrophobic interactions with lipid bilayers (**Fig. 1b**). The estimated length of hybridized Chol-DNAs is about 10.88 nm (32 base-pairs). The transmission electron microscope (TEM) images showed that the DNA NP was well folded with a high folding yield (**Fig.1c** and **Supplementary Fig. 1**) and the CNP binds to the surface of synthetic small lipid vesicles through hydrophobic interactions (**Fig. 1d**). To control the local concentration of cholesterols, we varied the spatial distribution of cholesterols to allow patterning 18- (0.005 cholesterols/nm^2), 36- (0.01

66 cholesterol/nm^2), or 72- (0.02 cholesterols/nm^2) cholesterols per a single NP, named as 18-CNP, 36-CNP,
67 and 72-CNP, respectively (**Fig. 1e**).

68

69 ***Formation of synthetic lipid rafts on T cell membranes***

70 Next, we examined whether these CNPs can drive the formation of lipid rafts by increasing the local
71 concentration of cholesterols on T cell membranes. Two different membrane binding strategies were
72 employed: (1) Chol-DNA, assist-DNA, and DNA NP was sequentially applied to Jurkat T cells
73 (**Supplementary Fig. 2a**); (2) CNPs were pre-assembled in a tube and added to T cells (**Fig. 1b**) as a single-
74 step reaction. Using both strategies, the addition of 72-CNP spontaneously formed micron-sized (~14.3 ±
75 5 μm in perimeter) polarized clusters, synthetic lipid rafts, on the T cell membranes (**Fig 2a, and**
76 **Supplementary Fig 2b**). The mean fluorescent intensity (MFI) of single cell-bound CNP was 3.4 times
77 higher in the single step binding reaction than it of the sequential reaction, indicating that direct treatment
78 of pre-complexed CNP is more efficient in membrane binding (**Supplementary Fig. 2c**). Next, to
79 investigate the impact of the nanoscale distribution of cholesterols on forming the CNP clusters and
80 polarization, we applied the CNP with different numbers of cholesterols (**Fig. 1e**). The NP without
81 cholesterol (0-chol) did not bind on Jurkat T cell membranes. CNP with more cholesterols showed higher
82 efficiency in the formation of polarized clusters of CNPs on the membrane (**Fig. 2b, c**). In CNP72-treated
83 samples, 69% of cells formed single-polarized synthetic lipid rafts on their membrane, and the percentages
84 of this single-polarized population dropped to 50% and 33% in 36-CNP- and 18-CNP-treated cells,
85 respectively. (**Fig. 2c, Supplementary Fig. 2d**). We also found that a minority of cells (< 5%) have more
86 than one polarized cluster (**Fig. 2c, Supplementary Fig. 2e**). Next, we tested the stability of CNP-induced
87 synthetic lipid rafts in a physiological condition and the effects on T cell proliferation. We found that T
88 cells treated with 72-CNP maintained the polarized caps of CNP for 4 hours while most of the 18- and 36-
89 CNPs detached from the cells, revealing that a higher local density of cholesterols enhances the stability of
90 synthetic lipid rafts (**Fig. 2d** and **Supplementary Fig. 3**). Binding of CNPs did not affect the proliferation
91 for 4 days regardless of the number of cholesterols on CNP (**Supplementary Fig. 4)**. The 72-CNP similarly
92 induced the formation of the synthetic lipid rafts in resting or effector primary mouse and human T cells
93 (**Fig. 2e, Supplementary Fig. 5a**), and these synthetic lipid rafts remained almost intact for 4 hours
94 (**Supplementary Fig. 5b, c**). Together, these results suggest that cholesterol-mediated binding of CNP
95 drives membrane segregation, and tighter cholesterol distribution on CNP enhances membrane binding
96 efficiency, synthetic lipid raft formation, and stability.

97

98 ***Synthetic lipid rafts are colocalized with Flot1-cap on T cells***

99 To characterize the nature of the CNP mediated synthetic lipid rafts on T cell membrane, we examined the
100 spatial organization and dynamics of the CNP and flotillin-1 (Flot1), a lipid raft associated protein [35,36].
101 Flot1 is known to segregate into lipid rafts by forming multimeric complexes at the inner leaflets [37,38]. In T
102 cells, Flot1 is weakly polarized on the membrane at the resting state and its polarization is enhanced by
103 stimulations [39-43]. Here, we formed synthetic lipid rafts using the 72-CNP on the Jurkat T cells stably
104 expressing Flot1 with Halo-tag at the C-terminus (Flot1-Halo). We monitored the dynamics of Flot1 for 30
105 minutes after adding the CNPs using fluorophore-conjugated Halo ligands. As reported previously, Flot1
106 formed cap-like membrane microdomains (**Fig 3a, b**), and it was more strongly polarized (50%) upon 72-
107 CNP addition than untreated controls (32.8%) (**Supplementary Fig. 6a**). CNP induced synthetic lipid rafts
108 showed high colocalization with Flot1-caps after 30 min incubation (the mean Pearson's correlation
109 coefficient (*R'*) and Manders overlap coefficient (*MOC*) were 0.63 ± 0.14 for both). The high colocalization
110 of the CNP clusters and Flot1-caps indicates the CNP mediated synthetic lipid raft can indeed mimic the
111 coalescence of lipid rafts (**Fig. 3c**). We observed three cases in live cell time-lapse imaging: (1) CNP
112 initially bound homogeneously on Flot1-unpolarized cells and it induced co-clustering of Flot1-caps and
113 CNP clusters (40 %) (**Supplementary Fig. 6b and Supplementary Movie 1**); (2) CNP initially bound
114 homogeneously on Flot1-polarized cells and moved to the Flot1 caps (33 %) (**Supplementary Fig. 6c and**
115 **Supplementary Movie 2**); (3) CNP was preferentially bound on the weakly polarized Flot1 cap and
116 enhanced the Flot1 cap polarization (27 %) (**Supplementary Fig. 6d and Supplementary Movie 3**).
117 Overall, CNP-mediated synthetic lipid rafts were highly colocalized Flot1 caps in T cells, and the binding
118 of CNP on the membrane further enhanced the polarization of Flot1, similar to when T cells activated by
119 anti-CD3/CD28, chemokines, or lipid raft crosslinking [41-43]. Interestingly the CNP is mostly bound on the
120 flat cell body but not on the microvilli of T cells (**Supplementary Fig. 7**).

121 It has been reported that the lateral mobility of Flot1-cap is significantly slower compared to the rest of
122 Flot1 in the non-cap area [39]. We monitored the lateral mobility of the 72-CNP on the Jurkat T cell membrane
123 using fluorescence recovery after photobleaching (FRAP). [44] Interestingly, there was almost no detectable
124 recovery of 72-CNP fluorescence in the synthetic lipid rafts for 5 minutes after rapid photobleaching.
125 (**Supplementary Fig. 8 and Supplementary Movie 4 and 5**). This result suggests that CNP formed highly
126 stable membrane domains exhibiting very slow diffusion. In contrast, there was a slow but gradual recovery
127 of Flot1 fluorescence reached a plateau after ~200 seconds in the synthetic lipid rafts (**Fig. 3d-f** and
128 **Supplementary Movie 5**). The diffusion coefficient (D) of Flot1 in the non-cap (non-raft) areas was ~2.1-
129 fold higher (D = 0.21 $\mu m^2 s^{-1}$) than D of Flot1 in the cap area (synthetic lipid raft) (D = 0.10 $\mu m^2 s^{-1}$) (**Fig.**
130 **3g**). There was a significant increase in D for Flot1 in the naturally formed polarized cap area (D = 0.15

131 $\mu m^2 s^{-1}$) compared to that for Flot1 in the synthetic lipid rafts induced by CNP binding (**Fig. 3g**). Together,
132 these results demonstrate that stable CNP clusters are formed at the outer leaflets, and these also stabilize
133 the lipid rafts on the inner leaflets of the membrane.

134

135 ***CD45 is excluded from the synthetic lipid raft***

136 CD45 exclusion from the immunological synapse (IS) is one of the crucial factors in T cell activation by
137 limiting abundant phosphatase activities [45-48]. It has been reported that artificially induced CD45 exclusion
138 can induce T cell activation without antigen [46]. Two models have proposed the CD45 exclusion mechanism:
139 the kinetic segregation model [49-51] and the lipid raft driven segregation model [17,24,52-54]. The former is ligation
140 dependent, explaining that CD45 is excluded from the close contacts due to the long extracellular domain
141 of CD45 (~23-50 nm) which is larger than the intermembrane junction formed by the TCR-pMHC
142 interaction (~15 nm) [49-51]. The latter is a ligation independent mechanism [17]. We examined whether CD45
143 is segregated from the CNP mediated synthetic lipid rafts independent of ligand association. Upon 72-CNP
144 addition, CD45 molecules partitioned away from the regions of the membrane where 72-CNP formed a
145 large synthetic lipid raft in the live T cell (**Fig. 4a, b**). The mean Pearson's *R'* and *MOC* between the CD45
146 and CNP obtained from 51 polarized cells were low as 0.18 ± 0.09 and 0.13 ± 0.07, respectively (**Fig. 4c**).
147 To quantify the level of exclusion, we segmented sub-areas of the cell membrane for the synthetic lipid raft
148 (raft, marked in yellow) and the non-raft (marked in light blue) regions (**Fig. 4d**) and calculated the
149 ratiometric intensity score (RIS) [17] between the CD45 and the CNP. RIS becomes zero when both molecules
150 have the same normalized intensities, +1 when CD45 is only present, and -1 when 72-CNP is only present.
151 The significant difference in RIS values between the raft (RIS= -0.67 ± 0.11) and the non-raft (RIS= +0.56
152 ± 0.16) areas indicate CD45 is excluded by CNP-mediated synthetic lipid rafts (**Fig. 4e, f)**. Furthermore,
153 the average intensity of CD45 within the synthetic raft was 66.9 % lower than that of CD45 localized in
154 non-raft regions (**Fig. 4g**). These results demonstrate that about two-thirds of CD45 molecules in a cell can
155 be segregated merely by lipid rafts on the T cell membrane without forming close contacts, supporting the
156 lipid raft mediated CD45 segregation model.

157

158 ***Synthetic lipid raft induces T cell activation***

159 We then investigated whether the CNP-mediated synthetic lipid raft can directly activate T cells without
160 any antigenic challenge. During early T cell activation, TCRs are accumulated at the core of IS [55], and
161 cholesterol can bind to TCRβ and induces TCR nanoclustering [56]. Thus, we tested whether the CNP can

recruit TCRs. In contrast to CD45, which was largely segregated away from the synthetic lipid rafts (**Fig. 4**), we could observe CD3 enrichment at the microdomains of CNP (**Fig. 5a, b**) in some cells. The average Pearson's *R* and *MOC* were 0.44±0.15 for both, and 37% of the analyzed cells (34 out of 92 cells) showed strong colocalization (*MOC* > 0.5) between TCR and CNP clusters (**Fig. 5c).** Wide variations in CD3 and CNP colocalization coefficients indicate that the efficiency of CD3 recruitment to the synthetic lipid rafts varies from cell to cell.

Next, we examined whether the CNP could transmit downstream TCR signals. Phosphorylation of cytosolic kinase TCR-zeta chain-associated 70-kDa tyrosine phosphoprotein (ZAP-70) is one of the early downstream TCR signaling [57,58]. We examined phosphorylation at tyrosine at 319-residue of ZAP-70 (ZAP-70 ^{Y319}) in the lysate of Jurkat T cells that were untreated or treated with 36- or 72-CNPs by immunoblot assay [59]. While 36-CNP treated cells showed only a modest and insignificant enhancement of ZAP-70 ^{Y319} phosphorylation (2.0 ± 0.76 folds), 72-CNP treatment induced a significant increase in phosphorylation of ZAP-70 ^{Y319} (2.7 ± 0.5 folds) compared to the basal level of phosphorylation in untreated cells (**Fig. 5d, e**).

We then monitored the surface expression of CD69 as an early cellular event indicative of T cell activation [60]. Jurkat T cells were incubated with 72-CNP or stimulated with PMA/ionomycin and analyzed for CD69 expression by flow cytometry. Although 72-CNP was less effective than PMA/ionomycin stimulation (37.9%), the percentages of CD69+ cells increased in the presence of 36-CNP (27.7%) and 72-CNP (33.7%) compared to untreated control (13%) after 4 hours of incubation (**Fig. 5f, g**). This indicates that the shorter inter-cholesterol spacing and higher cholesterol density on the CNP induced more efficient T cell activation in terms of the CD69 expression. In summary, these results demonstrate that the synthetic lipid rafts can activate T cells by recruiting TCRs while excluding CD45 and transmitting TCR signaling without specific antigenic challenges, and cholesterol density and patterning in the CNP affect the efficiency of downstream TCR signaling as well as CD69 expression in T cell activation.

Discussion

In this work, we have demonstrated a novel approach to create synthetic lipid rafts, large clusters of nanosized lipid raft-like monomers, on the T cell membranes that effectively drives membrane protein segregations and early T cell activation. Previous studies using model membranes composed of synthetic or cell membrane-derived lipids have demonstrated that high levels of cholesterols can induce a large-scale liquid-liquid phase separation (LLPS) of the lipids [12]. However, this micrometer scale membrane segregation formed by cholesterol has not been observed in the live cell membrane. Here, we developed a DNA origami-based cholesterol modification platform called CNP that permits facile control of the number, distance, or configuration of cholesterols on one side of DNA origami. The array of multiple cholesterols

195 on the CNP increased local concentration of cholesterols upon binding on the membrane, resembling the
196 nano-sized lipid raft monomer. The binding of CNPs drove a large-scale LLPS of the membrane, forming
197 a large synthetic lipid raft. The number of cholesterols linearly correlated to the formation of the segregation
198 of the domain. Our results suggest that the changes in local distribution of cholesterols shift the
199 thermodynamic equilibrium to form a large phase separation of the live cell membrane.

200 Another important enigma of the cell plasma membrane is the asymmetry between the two leaflets [61].
201 Although the physiological quantity of the cholesterols in the inner or outer leaflet is controversial [62], the
202 lipid composition of the outer leaflet lipid is known to be sufficient to form a lipid raft domain on the
203 membrane [63]. The lipid raft formation in the outer leaflet driven by cholesterol enrichment alters the spatial
204 distribution of other lipid components in the opposing leaflet, known as lipid-mediated transbilayer
205 coupling [63,64]. This may cause lipid raft formation on both sides of the plasma membrane and regulate T
206 cell signaling. In our system, we assume that the cholesterols complexed with the CNP exclusively insert
207 into the outer leaflet of the membrane because the bulky DNA origami structure is unlikely to undergo flip-
208 flop. A significantly decreased diffusion of Flot1 upon the CNP binding indicates that cholesterols in the
209 outer membrane can induce transbilayer coupling with the adjacent inner leaflet of the membrane. Our
210 nanotechnology platform can promote research efforts towards dissecting the mechanism driving
211 transbilayer coupling in T cells and expand our understanding of the roles of cholesterol-driven lipid rafts
212 in regulating T cell signaling.

213 Our results showed that ~67% of CD45 molecules were excluded from the synthetic lipid raft without
214 forming close contact with an APC. It strengthens the mechanism of lipid raft-driven partitioning of the
215 CD45 and supports the hypothesis that cholesterol is the cause of the segregation of CD45 [17]. The
216 incomplete segregation of CD45 in our study and the previously reported reconstitution study using
217 modification on length of ligations [65,66] may indicate that the CD45 exclusion at the IS is driven by both
218 lipid raft- and kinetic segregation mechanisms. We also demonstrated that the synthetic lipid raft
219 constructed with cholesterols could induce T cell activation without specific antigens. Note that although
220 we could observe TCR accumulation at the synthetic lipid rafts, some cells did not display TCR polarization
221 nor high colocalization with the CNP clusters. It could be partially caused by the fast internalization of the
222 TCR antibodies bound on the membrane or by the different localization efficiency on the microvilli-
223 localization [67]. The efficient TCR polarization might require other signaling mechanisms, such as actin
224 cytoskeleton rearrangement.

225 We found that the CNP is highly colocalized to the preassembled Flot1 cap on T cells. The preassembling
226 of the Flot1 cap is a unique feature found in hematopoietic cells [68]. It has been reported that Flot1
227 preassembled cap is resistant to cholesterol-disrupting agents [40]. Our results show that the assembly of Flot1

could be initiated and enhanced by the high local concentration of cholesterols. Also, once formed, the Flot1 clusters maintain their stability. The mechanism driving the preassembly of the Flot1 cap and the physiological roles of this spatially distinctive membrane remain poorly understood. The CNPs might serve as an optimal tool for dissecting the underlying mechanism of the Flot1 preassembly.

Our study reveals the critical role of cholesterols in mediating T cell signaling and function and the possibility of direct control of T cell activation using patterned cholesterols. Lipid rafts have been one of the controversial topics in biology for decades. Our strategy for controlling the spatial distribution of cholesterol can be easily substituted or extended with other major components of lipid rafts, such as sphingolipids or proteins. We anticipate that our strategy for forming and controlling synthetic lipid rafts can be widely applied and will become a versatile and powerful tool for studying the direct function of lipid rafts in various cell types.

References

1 Pike, L. J. Rafts defined: a report on the Keystone Symposium on Lipid Rafts and Cell Function. *J Lipid Res* **47**, 1597-1598, doi:10.1194/jlr.E600002-JLR200 (2006).

2 Simons, K. & Ikonen, E. Functional rafts in cell membranes. *Nature* **387**, 569-572, doi:10.1038/42408 (1997).

3 Lingwood, D. & Simons, K. Lipid Rafts As a Membrane-Organizing Principle. *Science* **327**, 46-50, doi:10.1126/science.1174621 (2010).

4 Sezgin, E., Levental, I., Mayor, S. & Eggeling, C. The mystery of membrane organization: composition, regulation and roles of lipid rafts. *Nature Reviews Molecular Cell Biology* **18**, 361-374, doi:10.1038/nrm.2017.16 (2017).

5 Stone, M. B., Shelby, S. A., Núñez, M. F., Wisser, K. & Veatch, S. L. Protein sorting by lipid phase-like domains supports emergent signaling function in B lymphocyte plasma membranes. *eLife* **6**, e19891, doi:10.7554/eLife.19891 (2017).

6 Varshney, P., Yadav, V. & Saini, N. Lipid rafts in immune signalling: current progress and future perspective. *Immunology* **149**, 13-24, doi:10.1111/imm.12617 (2016).

7 Sheng, R. *et al.* Cholesterol modulates cell signaling and protein networking by specifically interacting with PDZ domain-containing scaffold proteins. *Nature Communications* **3**, 1249, doi:10.1038/ncomms2221 (2012).

8 Levitan, I., Singh, D. & Rosenhouse-Dantsker, A. Cholesterol binding to ion channels. *Frontiers in Physiology* **5**, doi:10.3389/fphys.2014.00065 (2014).

9 Molnár, E. *et al.* Cholesterol and Sphingomyelin Drive Ligand-independent T-cell Antigen Receptor Nanoclustering*. *Journal of Biological Chemistry* **287**, 42664-42674, doi:https://doi.org/10.1074/jbc.M112.386045 (2012).

10 Igarashi, M., Honda, A., Kawasaki, A. & Nozumi, M. Neuronal Signaling Involved in Neuronal Polarization and Growth: Lipid Rafts and Phosphorylation. *Frontiers in Molecular Neuroscience* **13**, doi:10.3389/fnmol.2020.00150 (2020).

11 Wang, Y. *et al.* Cholesterol-Rich Lipid Rafts in the Cellular Membrane Play an Essential Role in Avian Reovirus Replication. *Frontiers in Microbiology* **11**, doi:10.3389/fmicb.2020.597794 (2020).

12 Crane, J. M. & Tamm, L. K. Role of cholesterol in the formation and nature of lipid rafts in planar and spherical model membranes. *Biophys J* **86**, 2965-2979, doi:10.1016/s0006-3495(04)74347-7 (2004).

13 McConnell, H. M. & Vrljic, M. Liquid-Liquid Immiscibility in Membranes. *Annual Review of Biophysics and Biomolecular Structure* **32**, 469-492, doi:10.1146/annurev.biophys.32.110601.141704 (2003).

14 Risselada, H. J. & Marrink, S. J. The molecular face of lipid rafts in model membranes. *Proceedings of the National Academy of Sciences* **105**, 17367-17372, doi:10.1073/pnas.0807527105 (2008).

15 Macdermaid, C. *et al.* Molecular dynamics simulations of cholesterol-rich membranes using a coarse-grained force field for cyclic alkanes. *The Journal of Chemical Physics* **143**, 243144, doi:10.1063/1.4937153 (2015).

16 Smondyrev, A. M. & Berkowitz, M. L. Structure of dipalmitoylphosphatidylcholine/cholesterol bilayer at low and high cholesterol concentrations: molecular dynamics simulation. *Biophys J* **77**, 2075-2089, doi:10.1016/S0006-3495(99)77049-9 (1999).

17 Jung, Y., Wen, L., Altman, A. & Ley, K. CD45 pre-exclusion from the tips of T cell microvilli prior to antigen recognition. *Nature Communications* **12**, 3872 (2021).

18 Bretscher, M. S. & Munro, S. Cholesterol and the Golgi Apparatus. *Science* **261**, 1280-1281, doi:10.1126/science.8362242 (1993).

19 Chichili, G. R., Westmuckett, A. D. & Rodgers, W. T cell signal regulation by the actin cytoskeleton. *J Biol Chem* **285**, 14737-14746, doi:10.1074/jbc.M109.097311 (2010).

20 Owen, D. M. *et al.* High plasma membrane lipid order imaged at the immunological synapse periphery in live T cells. *Molecular membrane biology* **27**, 178-189, doi:10.3109/09687688.2010.495353 (2010).

21 Gaus, K., Chklovskaia, E., Fazekas de St. Groth, B., Jessup, W. & Harder, T. Condensation of the plasma membrane at the site of T lymphocyte activation. *Journal of Cell Biology* **171**, 121-131, doi:10.1083/jcb.200505047 (2005).

22 Horejsí, V. Lipid rafts and their roles in T-cell activation. *Microbes Infect* **7**, 310-316, doi:10.1016/j.micinf.2004.12.004 (2005).

23 Kabouridis, P. S. Lipid rafts in T cell receptor signalling. *Molecular membrane biology* **23**, 49-57, doi:10.1080/09687860500453673 (2006).

24 Rodgers, W. & Rose, J. K. Exclusion of CD45 inhibits activity of p56lck associated with glycolipid-enriched membrane domains. *Journal of Cell Biology* **135**, 1515-1523, doi:10.1083/jcb.135.6.1515 (1996).

25 Bietz, A., Zhu, H., Xue, M. & Xu, C. Cholesterol Metabolism in T Cells. *Front Immunol* **8**, 1664, doi:10.3389/fimmu.2017.01664 (2017).

26 Surls, J. *et al.* Increased Membrane Cholesterol in Lymphocytes Diverts T-Cells toward an Inflammatory Response. *PLOS ONE* **7**, e38733, doi:10.1371/journal.pone.0038733 (2012).

27 Kabouridis, P. S., Janzen, J., Magee, A. L. & Ley, S. C. Cholesterol depletion disrupts lipid rafts and modulates the activity of multiple signaling pathways in T lymphocytes. *European Journal of Immunology* **30**, 954-963, doi:https://doi.org/10.1002/1521-4141(200003)30:3<954::AID-IMMU954>3.0.CO;2-Y (2000).

28 Yang, W. *et al.* Potentiating the antitumour response of CD8+ T cells by modulating cholesterol metabolism. *Nature* **531**, 651-655, doi:10.1038/nature17412 (2016).

29 Pathan-Chhatbar, S. *et al.* Direct Regulation of the T Cell Antigen Receptor's Activity by Cholesterol. *Frontiers in Cell and Developmental Biology* **8**, doi:10.3389/fcell.2020.615996 (2021).

316 30 Swamy, M. *et al.* A Cholesterol-Based Allostery Model of T Cell Receptor Phosphorylation.
317 *Immunity* **44**, 1091-1101, doi:https://doi.org/10.1016/j.immuni.2016.04.011 (2016).
318 31 Chen, Y. *et al.* Cholesterol inhibits TCR signaling by directly restricting TCR-CD3 core tunnel
319 motility. *Mol Cell* **82**, 1278-1287.e1275, doi:10.1016/j.molcel.2022.02.017 (2022).
320 32 Douglas, S. M. *et al.* Self-assembly of DNA into nanoscale three-dimensional shapes. *Nature* **459**,
321 414-418 (2009).
322 33 Rothemund, P. W. K. Folding DNA to create nanoscale shapes and patterns. *Nature* **440**, 297-302
323 (2006).
324 34 Ficht, X. *et al.* In Vivo Function of the Lipid Raft Protein Flotillin-1 during CD8+ T Cell–Mediated
325 Host Surveillance. *The Journal of Immunology* **203**, 2377-2387, doi:10.4049/jimmunol.1900075
326 (2019).
327 35 Ficht, X. *et al.* In Vivo Function of the Lipid Raft Protein Flotillin-1 during CD8(+) T Cell-Mediated
328 Host Surveillance. *J Immunol* **203**, 2377-2387, doi:10.4049/jimmunol.1900075 (2019).
329 36 Yokoyama, H. & Matsui, I. The lipid raft markers stomatin, prohibitin, flotillin, and HflK/C (SPFH)-
330 domain proteins form an operon with NfeD proteins and function with apolar polyisoprenoid
331 lipids. *Crit Rev Microbiol* **46**, 38-48, doi:10.1080/1040841x.2020.1716682 (2020).
332 37 Otto, G. P. & Nichols, B. J. The roles of flotillin microdomains--endocytosis and beyond. *J Cell Sci*
333 **124**, 3933-3940, doi:10.1242/jcs.092015 (2011).
334 38 Kwiatkowska, K., Matveichuk, O. V., Fronk, J. & Ciesielska, A. Flotillins: At the Intersection of
335 Protein S-Palmitoylation and Lipid-Mediated Signaling. *International Journal of Molecular*
336 *Sciences* **21** (2020).
337 39 Langhorst, M. F. *et al.* Preformed reggie/flotillin caps: stable priming platforms for macrodomain
338 assembly in T cells. *The FASEB Journal* **20**, 711-713, doi:https://doi.org/10.1096/fj.05-4760fje
339 (2006).
340 40 Rajendran, L. *et al.* Asymmetric localization of flotillins/reggies in preassembled platforms
341 confers inherent polarity to hematopoietic cells. *Proceedings of the National Academy of*
342 *Sciences* **100**, 8241-8246, doi:10.1073/pnas.1331629100 (2003).
343 41 Affentranger, S., Martinelli, S., Hahn, J., Rossy, J. & Niggli, V. Dynamic reorganization of flotillins
344 in chemokine-stimulated human T-lymphocytes. *BMC Cell Biology* **12**, 28, doi:10.1186/1471-
345 2121-12-28 (2011).
346 42 Giri, B. *et al.* CXCL12-induced partitioning of flotillin-1 with lipid rafts plays a role in CXCR4
347 function. *Eur J Immunol* **37**, 2104-2116, doi:10.1002/eji.200636680 (2007).
348 43 Slaughter, N. *et al.* The flotillins are integral membrane proteins in lipid rafts that contain TCR-
349 associated signaling components: implications for T-cell activation. *Clin Immunol* **108**, 138-151,
350 doi:10.1016/s1521-6616(03)00097-4 (2003).
351 44 Axelrod, D., Koppel, D. E., Schlessinger, J., Elson, E. & Webb, W. W. Mobility measurement by
352 analysis of fluorescence photobleaching recovery kinetics. *Biophysical Journal* **16**, 1055-1069,
353 doi:https://doi.org/10.1016/S0006-3495(76)85755-4 (1976).
354 45 Courtney, A. H. *et al.* CD45 functions as a signaling gatekeeper in T cells. *Science Signaling* **12**,
355 eaaw8151, doi:10.1126/scisignal.aaw8151 (2019).
356 46 James, J. R. & Vale, R. D. Biophysical mechanism of T-cell receptor triggering in a reconstituted
357 system. *Nature* **487**, 64-69, doi:10.1038/nature11220 (2012).
358 47 Sibener, L. V. *et al.* Isolation of a Structural Mechanism for Uncoupling T Cell Receptor Signaling
359 from Peptide-MHC Binding. *Cell* **174**, 672-687.e627, doi:10.1016/j.cell.2018.06.017 (2018).
360 48 Varma, R., Campi, G., Yokosuka, T., Saito, T. & Dustin, M. L. T cell receptor-proximal signals are
361 sustained in peripheral microclusters and terminated in the central supramolecular activation
362 cluster. *Immunity* **25**, 117-127, doi:10.1016/j.immuni.2006.04.010 (2006).

49 Wild, M. K. *et al.* Dependence of T Cell Antigen Recognition on the Dimensions of an Accessory Receptor–Ligand Complex. *Journal of Experimental Medicine* **190**, 31-42, doi:10.1084/jem.190.1.31 (1999).
50 Davis, S. J. & van der Merwe, P. A. The structure and ligand interactions of CD2: implications for T-cell function. *Immunology Today* **17**, 177-187, doi:https://doi.org/10.1016/0167-5699(96)80617-7 (1996).
51 Shaw, A. S. & Dustin, M. L. Making the T cell receptor go the distance: a topological view of T cell activation. *Immunity* **6**, 361-369, doi:10.1016/s1074-7613(00)80279-4 (1997).
52 Hořejší, V. Lipid rafts and their roles in T-cell activation. *Microbes and Infection* **7**, 310-316, doi:https://doi.org/10.1016/j.micinf.2004.12.004 (2005).
53 Janes, P. W., Ley, S. C., Magee, A. I. & Kabouridis, P. S. The role of lipid rafts in T cell antigen receptor (TCR) signalling. *Semin Immunol* **12**, 23-34, doi:10.1006/smim.2000.0204 (2000).
54 Zhang, M. *et al.* CD45 Signals outside of Lipid Rafts to Promote ERK Activation, Synaptic Raft Clustering, and IL-2 Production1. *The Journal of Immunology* **174**, 1479-1490, doi:10.4049/jimmunol.174.3.1479 (2005).
55 Grakoui, A. *et al.* The immunological synapse: a molecular machine controlling T cell activation. *Science* **285**, 221-227, doi:10.1126/science.285.5425.221 (1999).
56 Molnár, E. *et al.* Cholesterol and sphingomyelin drive ligand-independent T-cell antigen receptor nanoclustering. *J Biol Chem* **287**, 42664-42674, doi:10.1074/jbc.M112.386045 (2012).
57 Wang, H. *et al.* ZAP-70: an essential kinase in T-cell signaling. *Cold Spring Harb Perspect Biol* **2**, a002279, doi:10.1101/cshperspect.a002279 (2010).
58 Chan, A. C. & Shaw, A. S. Regulation of antigen receptor signal transduction by protein tyrosine kinases. *Current Opinion in Immunology* **8**, 394-401, doi:https://doi.org/10.1016/S0952-7915(96)80130-0 (1996).
59 Di Bartolo, V. *et al.* Tyrosine 319, a newly identified phosphorylation site of ZAP-70, plays a critical role in T cell antigen receptor signaling. *J Biol Chem* **274**, 6285-6294, doi:10.1074/jbc.274.10.6285 (1999).
60 Ziegler, S. F., Ramsdell, F. & Alderson, M. R. The activation antigen CD69. *Stem Cells* **12**, 456-465, doi:10.1002/stem.5530120502 (1994).
61 Bretscher, M. S. Asymmetrical Lipid Bilayer Structure for Biological Membranes. *Nature New Biology* **236**, 11-12, doi:10.1038/newbio236011a0 (1972).
62 Steck, T. L. & Lange, Y. Transverse distribution of plasma membrane bilayer cholesterol: Picking sides. *Traffic* **19**, 750-760, doi:https://doi.org/10.1111/tra.12586 (2018).
63 Kiessling, V., Crane, J. M. & Tamm, L. K. Transbilayer Effects of Raft-Like Lipid Domains in Asymmetric Planar Bilayers Measured by Single Molecule Tracking. *Biophysical Journal* **91**, 3313-3326, doi:https://doi.org/10.1529/biophysj.106.091421 (2006).
64 Raghupathy, R. *et al.* Transbilayer lipid interactions mediate nanoclustering of lipid-anchored proteins. *Cell* **161**, 581-594, doi:10.1016/j.cell.2015.03.048 (2015).
65 James, J. R. & Vale, R. D. Biophysical mechanism of T-cell receptor triggering in a reconstituted system. *Nature* **487**, 64-69, doi:10.1038/nature11220 (2012).
66 Carbone, C. B. *et al.* In vitro reconstitution of T cell receptor-mediated segregation of the CD45 phosphatase. *Proceedings of the National Academy of Sciences* **114**, E9338-E9345, doi:10.1073/pnas.1710358114 (2017).
67 Jung, Y. *et al.* Three-dimensional localization of T-cell receptors in relation to microvilli using a combination of superresolution microscopies. *Proceedings of the National Academy of Sciences* **113**, E5916-E5924, doi:10.1073/pnas.1605399113 (2016).
68 Rajendran, L. *et al.* Flotillins Are Involved in the Polarization of Primitive and Mature Hematopoietic Cells. *PLOS ONE* **4**, e8290, doi:10.1371/journal.pone.0008290 (2009).

411 69 Dong, R. *et al.* DNA origami patterning of synthetic T cell receptors reveals spatial control of the
412 sensitivity and kinetics of signal activation. *Proceedings of the National Academy of Sciences*
413 **118**, e2109057118 (2021).
414 70 Douglas, S. M. *et al.* Rapid prototyping of 3D DNA-origami shapes with caDNAno. *Nucleic acids*
415 *research* **37**, 5001-5006 (2009).
416 71 Stahl, E., Martin, T. G., Praetorius, F. & Dietz, H. Facile and scalable preparation of pure and
417 dense DNA origami solutions. *Angewandte Chemie* **126**, 12949-12954 (2014).
418 72 Ohmann, A. *et al.* Controlling aggregation of cholesterol-modified DNA nanostructures. *Nucleic*
419 *acids research* **47**, 11441-11451 (2019).
420 73 Ellenberg, J. *et al.* Nuclear membrane dynamics and reassembly in living cells: targeting of an
421 inner nuclear membrane protein in interphase and mitosis. *J Cell Biol* **138**, 1193-1206,
422 doi:10.1083/jcb.138.6.1193 (1997).
423 74 Rodgers, J. L. & Nicewander, W. A. Thirteen Ways to Look at the Correlation Coefficient. *The*
424 *American Statistician* **42**, 59-66, doi:10.2307/2685263 (1988).
425 75 Manders, E. M. M., Verbeek, F. J. & Aten, J. A. Measurement of co-localization of objects in dual-
426 colour confocal images. *Journal of Microscopy* **169**, 375-382, doi:10.1111/j.1365-
427 2818.1993.tb03313.x (1993).

428

429

430 **Methods**

431 **Synthesizing the cholesterol nano-patch (CNP)**

432 The DNA nano-patch (NP) was designed on the honeycomb lattice with a long sing-stranded scaffold, type
433 p8064 (Tilibit), by modifying the structure of R. Dong et al. [69] Sequence of 183 staple strands of the DNA
434 NP was determined using the open-source program, caDNAno,[70] (Supplementary Table S1) and the
435 corresponding staple strands were synthesized from Bioneer. A folding mixture consists of 20 nM of
436 scaffold DNA, 100 nM of each staple strands, 20 mM $MgCl_2$ and 5 mM NaCl in TE buffer (5 mM Tris and
437 1 mM EDTA, pH 8). The annealing was performed following a temperature profile: 70 °C for 15 min, 60
438 to 20 °C by 1 °C/ho in a thermocycler. Excessive staple strands were removing by polyethylene glycol
439 (PEG) precipitation [71] followed by two rounds of ultrafiltration with a 100 kDa cut-off filter. A
440 concentration of the DNA NP was measured using UV spectrometer and adjusted using the working buffer
441 (1×TE, 10 mM of $MgCl_2$, and 5 mM of NaCl). Purified samples were stored at 4 °C. To form the Chol-
442 patch, we mixed the DNA NP with four-fold excessive assist-DNAs and Chol-DNAs to the total number
443 of DNA handle on the DNA NP and incubated them at 30 °C for 12 h. At the 3' end of assist-DNAs, a six-
444 nucleotides-thymine (6T) is appended to minimize undesired hydrophobic interaction between Chol-DNAs
445 by wrapping the neighboring cholesterol [72]. To remove undesired hydrophobic interactions, Chol-DNA was
446 heated at 65 °C for 1 h before use. The mixed solution was purified by ultrafiltration with a 100 kDa cut-
447 off filter using phenol red free RPMI (Gibco) (buffer and its concentration was adjusted using the phenol
448 red free RPMI.

449

450 **Agarose gel electrophoresis**

451 The assembled CNP was electrophoresed using 1% agarose gel containing 0.5×TBE (45 mM Tris-borate
452 and 1 mM EDTA), 10 mM of $MgCl_2$ and 0.1 $ul \cdot ml^{-1}$ of SYBR Safe (Thermofisher). Electrophoresis was

453 performed for 90 min at 70 V bias voltage in a cold room. Agarose gel was scanned by a GelDoc and Image
454 Lab v5.1 program (Bio-Rad)

455

456 **TEM Imaging**

457 The concentration of CNP was diluted to 3 nM with the working buffer. The sample solution (5 μL) was
458 deposited on a glow-discharged formvar-supported carbon-coated grid for 3 min and stained by a 2% uranyl
459 formate and 25 mM NaOH for 40 sec. TEM images were taken at 40k-fold magnification using JEM-
460 2100Plus (JEOL).

461

462 **Tissue culture**

463 Jurkat T cells (Clone E6-1, ATCC) or Flot1-Halo transduced Jurkat T cells were grown in complete RPMI
464 (Gibco) media containing 2 mM L-glutamine, 100 U penicillin-streptomycin (PS) (Gibco) and 10% FBS
465 (Gibco). Human pan T cells were purified from frozen peripheral blood mononuclear cells (PBMCs,
466 STEMCELL Technologies, Cat #70025.2. Lot 201671701C) using a negative selection human Pan T Cell
467 Isolation Kit (Miltenyi Biotec) and mouse T cells were purified from mouse splenocytes using a negative
468 selection EasySep™ Mouse T Cell Isolation Kit (STEMCELL Technologies). Mouse splenocytes were
469 prepared from spleens collected from 8-18 weeks old male BL6 mice purchased from Orient bio. For each
470 experiment, a spleen was processed through a 40 μm filter (STEMCELL Technologies) and RBCs were
471 removed from the single cell suspension using RBC lysis buffer (eBioscience). Freshly isolated resting cells
472 for both human and mouse were used after incubation in complete T cell media, containing 10% (v/v) FBS,
473 100 U PS, 1x GlutaMAX supplement (Gibco), 1mM sodium pyruvate (Sigma Aldrich) and 1x nonessential
474 amino acids solution (Sigma Aldrich) in RPMI for ~2-4 h in a CO_2 (5%) incubator at 37 °C. For human
475 effector T cells, purified pan T cells were cultured with human anti-CD3/anti-CD28 dynabeads (Gibco) at

476 a 2:1 ratio in the complete T cell media supplementing with 50μM 2-mercaptoethanol and 100 $U \cdot mL^{-1}$ of
477 IL-2 upto a week.

478 **Sample preparation for imaging**

479 Jurkat or primary T cells were washed with calcium and magnesium free PBS (Gibco) by centrifugation at
480 200 g for 5 min (spin wash) and then resuspended in phenol red free RPMI. For the sequential reaction,
481 cells were spin washed and then incubated with 10 μM of Chol-DNAs for 10min at 37 °C. After spin
482 washing, 10 μM of DNA assist-DNAs was added and incubated for 10 min and then 10 nM of DNA NP
483 (containing 72-anchors) was added to the sample. The unbound DNAs are removed by a spin wash. For
484 the single step reaction, Chol- DNAs were complexed with DNA NP prior to use and then directly added
485 the CNP to spin washed cells at a final concentration of 10 nM in total 50 μl of phenol red free RPMI and
486 incubated in a CO_2 (5%) incubator for 30 min at 37 °C, otherwise, the incubation time was indicated. Cells
487 were spin washed with PBS, ready for using live cell imaging. For nuclei staining, cells were fixed with 4 %
488 (w/v) paraformaldehyde (PFA) (Electron Microscopy Sciences) in PBS for 15 min at Room temperature
489 (RT) and washed in PBS. Cells were stained with 10 uM of Hoechst 33342 (Thermo Fisher Scientific) for
490 5 min and then washed with PBS. For Flot1-Halo labeling, after washing cells with PBS, cells were stained
491 with Janelia Fluor (JF) 549 conjugated Halotag ligands (Promega) at 200 nM concentration in 2% FBS/PBS
492 at 37 °C for 15 min. The unbound Halo tags were spin washed with PBS and then cells were incubated with
493 CNP for 30 min, as described above. For CD45 labeling, the CNP labeled cells were washed and blocked
494 with 2% BSA in PBS for 10 min in the placed in a poly L- lysine (PLL) coated glass bottom chamber and
495 then labeled with $1ug \cdot ml^{-1}$ of Alexa Flour (AF) 488 conjugated anti-human CD45 antibodies (Biolegend,
496 Cat# 304017, clone HI30) in 2% BSA in PBS for 20 min at RT. Cells were gently rinsed with PBS 4 times.
497 For CD3 labeling, the CNP labeled cells were spin washed and incubated with $10\mu g \cdot ml^{-1}$ of AF488
498 conjugated anti-CD3 antibodies (Biolegend, Cat # 300415, clone UCHT1) in 2% BSA/PBS on ice for
499 30min and then spin washed. For imaging, 70~100 μl of freshly prepared cells resuspended in PBS were
500 PLL (0,01 %, Sigma Aldrich) or collagen ($50\ mg \cdot ml^{-1}$, Corning) coated glass-bottom chamber (35 mm dish,

501 7 mm glass, MatTek). The chambers were freshly prepared prior to use. For live time-lapse imaging,
502 Halotag labeled cells resuspended in phenol red free RPMI were placed on the PLL coated glass bottom
503 chamber and then 3~5 ul of CNP in RPMI were added and mixed to a final concentration of 3~5nM. Image
504 acquisitions were started 2 min after adding the CNP.

505 **Plasmid construction and lentiviral transduction**

506 The lentiviral pLV-FLOT1-Halo plasmid (gifted from Prof. Young-Wook Jun at the University of
507 California San Francisco) and two packaging plasmids pSPAX2 (Addgene) and pMD2.G (Addgene) were
508 cotransfected into Lenti-X293T cells (Takara) using lipofectamine 2000 (Thermo Fisher Scientific)
509 following the manufacturer's instructions. The supernatant was collected and filtered after 48 h using a 0.45
510 µm pore sized Millex PVDF syringe filter (Millipore). The filtered virus was concentrated by
511 ultracentrifugation at 10,000 g for 2 h and then applied to Jurkat T cells for two days. The transduced Jurkat
512 T cells were spin washed and maintained in complete RPMI media for three days and harvested for sorting.
513 The sorted Flot1-Halo transduced cells were cultured in complete T cell media for two days and maintained
514 in complete RPMI media.

515 **Flow cytometry**

516 The bindings of DNA NP with or without cholesterol modification on a single cell were analyzed using
517 flow cytometry. After 30 min incubation with DNA NP or CNP, cells were either washed or added 1 ml of
518 complete RPMI media and incubated for 4 h at 37 °C in a CO_2 (5%) incubator. The harvested cells incubated
519 for 30 min or 4 h were spin washed with PBS and stained with LIVE/DEAD™ Fixable Violet Dead Cell
520 Stain dye (L/D violet) (Invitrogen) diluted in PBS (1:1000) for 10 min at RT in dark. Cells were spin washed
521 and loaded on a Fusion cell sorter (BD Biosciences). Single cells were gated using forward vs. side scatter
522 (FSC vs. SSC) and then the live cells gated for the negative population of the L/D violet were analyzed for
523 the Cy5 fluorescence on CNP using FlowJo (BD Biosciences, versions 10.8.1) software. For CD69
524 expression analysis, cells were incubated without or with CNP, or PMA (10 $ng \cdot ml^{-1}$) (Sigma Aldrich) and

525 ionomycin (0.5 μg·ml^{-1}) (Sigma Aldrich) in RPMI for 30 min at 37 °C, then 1 ml of complete RPMI was
526 added and incubated for 4 h at 37 °C in a CO_2 (5 %) incubator. Cells were harvested and spin washed with
527 PBS and then labeled with L/D violet for 10 min at RT. Cells were spin washed with 2% FBS/PBS and
528 then resuspended in 100 µl of 2 % FBS/PBS, followed by staining with Brilliant Violet (BV) 785 conjugated
529 anti-human CD69 (10 μg·ml^{-1}) (Biolegend, Cat # 310932, clone FN50) for 30 min on ice. Cells were spin
530 washed and loaded on a FACSAria Fusion cytometer (BD Biosciences). For compensation, ArC amine
531 reactive compensation bead (Invitrogen) stained with L/D violet and UltraComp eBeads (Invitrogen)
532 stained with AF 647 conjugated anti-IgG antibody for Cy5 or the BV785 conjugated CD69 antibody in
533 PBS were used. The live single cell, CD69 positive population was analyzed using the FlowJo software.
534 For cell proliferation tracking analysis, Jurkat T cells were harvested and spin washed in PBS and stained
535 with Cell Tracker Green CMFDA (1 µM) (Invitrogen) diluted in 2% FBS/PBS for 20 min at 37 °C in a CO_2
536 (5 %) incubator. After spin washing with 2 % FBS/PBS, cells were resuspended in RPMI and incubated
537 without or with 36- or 72-CNP at 10 nM for 30 min at 37 °C in a CO_2 (5 %) incubator. Cells were spin
538 washed (day 0 sample) or were grown in complete RPMI media for 5 days. Cells were harvested and
539 analyzed the diluted intensities of the CMFDA every day (day 0–day 4) by flow cytometry. After spin wash
540 the harvest cells, cells were stained with L/D violet in PBS (1:1000) for 10 min at RT. Cells were rinsed
541 with PBS and then loaded on the cytometer. The distribution of the intensities of the CMFDA on the live
542 Jurkat T cells was analyzed using the FlowJo software.

543 **Fluorescence-activated single cell sorting (FACS)**

544 For sorting, the Flot1-Halo transduced cells were spin washed with PBS and stained with L/D violet (1:1000)
545 for 10 min at RT. After spin washing, cells were stained with JF549 conjugated Halotag ligands (Promega)
546 at 200nM concentration in 2% FBS/PBS for 20 min at RT, followed by spin washing with 2 % FBS/PBS.
547 The cells were resuspended in 2 % FBS/PBS and kept on ice in the dark. Cells were immediately loaded
548 for sorting on a Fusion cell sorter (BD Bioscience). Live single cells were gated as described above and

549 then the JF549 labeled Flot1-Halo positive cells were analyzed and sorted using FACSDiva software (BD
550 Biosciences, version 8.0.2).

551 **Confocal imaging**

552 Confocal images were taken with a laser scanning Ti Microscope (Nikon) using an Apo 60 x Oil λS DIC
553 N2 objective lens (N.A., 1.4) (Nikon) with a 46~52 μm sized pinhole. 4 laser lines at 405, 488, 561, and
554 633 nm, and a combination of filter sets (dichroic: BS 20/80, emission bandpass: 450/50, 525/50, 595/50
555 and 700/75) were used for taking 9-20 series of z-plane confocal images with a step of 0.5 or 1 μm for the
556 Hoechst, AF488-, JF549- and Cy5-labeled samples, respectively. Bright field images were taken with a
557 transmission detector.

558 **FRAP analysis**

559 For FRAP experiments, time lapse confocal images were acquired using a Zeiss LSM 900 (Zeiss)
560 microscope, equipped with a C-Apochromat 40x Water Korr (N.A. 1.2) (Zeiss) objective lens with a 50 μm
561 sized pinhole. 561-, or 633-nm laser lines were used to excite, and bleach and emission fluorescence
562 between 400-635 nm and 645-700 nm were collected for the JF549-Flot1-Halo and Cy5-labeled CNP,
563 respectively. Time lapse series images were taken for 5 min with 3 s or 10 s intervals. After taking 3-5
564 frame images, a squared area of 0.5 μm^2 was selected and bleached for 3 s with 80 % of power for each
565 laser line. Drifting and motility of cells during the measurement were corrected that each frame image was
566 corrected to the next frame image except for the bleached frame using the 'imregtform' function (optimizer:
567 'rigid') in Matlab. The trace of the mean fluorescence intensities of the bleached area in the time-lapse
568 movie was analyzed using a custom-written Matlab (MathWorks, version R2018a) script. The diffusion
569 coefficient (*D*) for Flot1 was determined by analyzing the fluorescence recovery trace for 2.5 min after
570 bleaching using the following equation [73]: $\mathrm{I(t)} = I_t = I_{final}\,(1 - (\omega^2\,(\omega^2 + 4\pi Dt)^{-1})^{1/2}$, where I_t is
571 intensity as a function of time, I_{final} is final intensity reached after recovery, ω is width of the bleached

572 area, and D is one dimensional diffusion coefficient, which was determined by fitting using a built-in
573 function in Matlab.

574 **Image analysis**

575 ImageJ (version 1.52p) and Matlab (MathWorks, version R2018a) were used for image processing. For
576 counting the polarization population, each population of cells was counted from the maximum intensity
577 projection of 9-11 z-stack images using an ImageJ built in function, cell counter. The perimeters of the
578 single polarized clusters were manually measured from a z plane of the middle of each cell in the confocal
579 images using image J. For the colocalization test between channel X and channel Y, Pearson's correlation
580 coefficient [74] ($R' = \frac{\sum_{i=1}^{n}(X_i-\bar{X})(Y_i-\bar{Y})}{\sqrt{\sum_{i=1}^{n}(X_i-\bar{X})^2}\sqrt{\sum_{i=1}^{n}(Y_i-\bar{Y})^2}}$, where n is the total number of pixels, X_i and Y_i are the pixel
581 intensities indexed with i. $\bar{X}$ and $\bar{Y}$ is the mean intensity of X and Y images, respectively) and Manders'
582 overlap coefficient [75] (
583 $MOC = \frac{\sum_{i=1}^{n}(x_i)(y_i)}{\sqrt{\sum_{i=1}^{n}(x_i)^2}\sqrt{\sum_{i=1}^{n}(y_i)^2}}$, where n is the total number of pixels, x_i and y_i are the intensities of above-
584 threshold pixels indexed i in the X and Y images) were calculated using a custom built Matlab script. For
585 MOC, the first threshold values obtained using the 'multithresh' function in Matlab were used. For
586 quantifying the CD45 segregation, ratiometric intensity score (RIS) was calculated by following equation
587 [17] : $RIS = (X_i - Y_i\,(\bar{X}/\bar{Y}))/(X_i + Y_i(\bar{X}/\bar{Y}))$, where X_i and Y_i are the intensity of each pixel indexed i for
588 channel X (CD45) and channel Y (72-CNP); $\bar{X}$ and $\bar{Y}$ represent the mean of total X and Y, respectively. The
589 RIS and the mean intensities of CD45 for the raft and non-raft area were analyzed with data within the
590 segmented area presented in Fig. 4d. The original intensity values were used without subtracting
591 background for R', RIS, and CD45 intensity calculations. For the CD45 intensity plot in Fig. 4g, the
592 intensity of the segmented area for CD45 was normalized to 0-1 value for each cell and then it was
593 normalized to the mean of the non-raft intensities of all analyzed cells. The region of interest (ROI) for
594 induvial cells was selected by ImageJ or Matlab script. The raft and non-raft area of the CD45 and 72-CNP

595 dual-labeled images were segmented using a custom-written Matlab script. Briefly, channel 1 (CD45) and
596 channel 2 (72-CNP) images and the summed images of these two were binarized as BW1, BW2, and BW3
597 using the first threshold obtained from the 'multithresh' function in Matlab. The noise elements (less than
598 10 connected components) were removed from the BW3 using the 'bwconncomp' function. Next,
599 morphological closing was performed using the 'imclose' function on the nonzero element of the BW2 and
600 BW3 for the raft area, and on the nonzero element of the BW1 and BW3 for the non-raft area. Any element
601 that is less than 10 connected components was removed from the raft or non-raft areas using the
602 'bwconncomp' function. The nonzero element of raft or non-raft became the total segmented area. To
603 eliminate the boundary regions, any nonzero values of the raft area overlapped with the dilated non-raft
604 area using the 'imdilate' function with a disk structuring element with a radius of 10 pixels were removed.

605 The display ranges of the intensities of individual color channels in **Fig. 2**, **Fig. 3f**, **Supplementary Figs.**
606 **2, 3, and 5** were independently optimized using ImageJ or Matlab. However, for comparison, the display
607 ranges of Cy5 intensity in Supplementary **Fig. 2b** were adjusted to that of **Fig. 2a**; the 0-, 18- and 36- CNP
608 images in **Fig. 2b** and **Supplementary Fig. 3** were adjusted to the 72-CNP image in **Fig. 2b**; Supplementary
609 **Fig. 5a** was adjusted to the **Fig. 2e**. The display ranges of the all figures in Supplementary **Fig. 6** and
610 **Supplementary Movies 1-3** were equal and all other images in this study were displayed between the 1%
611 ~ 99% intensity of individual channel image using a built-in function in Matlab.

612 **Immunoblotting assay**

613 Jurkat T cells were incubated with 10 nM of 72-CNP in RPMI for 30min at 37 °C. Cells were spin washed
614 with ice-cold PBS and lysed in lysis buffer containing 20 mM HEPES (pH 7.0), 1 % Triton X-100, 150
615 mM NaCl, 10 % glycerol, 1 mM EDTA, 2 mM EGTA, 1x Protease Inhibitor cocktail (Cell Signaling
616 Technology) and 1x phosphatase inhibitor cocktail (Cell Signaling Technology). Cell lysates were
617 centrifuged at 12,000 g for 10 min, and the protein concentrations were determined by Bradford assay (Bio-
618 Rad). Protein samples were mixed with SDS sample buffer containing 312.5 mM Tris (pH6.8), 10 % SDS,
619 30 % glycine, $1 mg \cdot ml^{-1}$ bromophenol blue and 1 M 2-mercaptoethanol, and boiled for 5 min. The proteins

620 were separated by SDS-PAGE and transferred to nitrocellulose membranes by electroblotting for 1 h 30
621 min. The membranes were blocked with 5 % dry skimmed milk in Tris-buffered saline containing 0.05 %
622 (v/v) Tween-20 (TBST) for 1 h and incubated with rabbit anti-phospho Zap-70(Tyr319)/ Syk (Tyr352)
623 (Cell Signaling Technology, Cat # 2717T, Clone 65E4), anti-β actin antibody (Cell Signaling Technology,
624 Cat # 4970, clone 13E5), or anti-α-tubulin antibody (Sigma Aldrich, Cat #T5168, Clone B-5-1-2) diluted
625 in the blocking buffer (1:1000) for overnight at 4 °C. After washing 3 times with TBST, the membranes
626 were incubated with HRP conjugated anti-rabbit IgG secondary antibody (Cell Signaling Technology, Cat
627 #7074) diluted in blocking buffer (1:2000) for 1 h at RT and the washed with TBST 3 times. The immune-
628 reactive bands were detected using an enhanced chemiluminescence kit (Sigma Aldrich) and ChemiDoc
629 imaging system (Bio-Rad) and quantified with ImageJ software (version 1.52p).

630

631 **Statistical information**

632 At least three independent experiments were performed except **Supplementary Fig. 2 b-c, Fig. 4**, (two
633 independent experiments) and the statistical details for each experiment are indicated in the figure legends.
634 The p-values, mean, standard deviation (SD), and standard error of the mean (SE) were determined using
635 the built-in functions in Matlab (MathWorks, R2018a) or Prism 8 (GraphPad, version 8.0.1).

636

637 **Data availability**

638 The sequences for the DNA structures are listed in the Supplementary Table1. Data that are generated and
639 used in this study are available from the corresponding author upon reasonable request.

640

641 **Code availability**

642 Custom Matlab codes used in this study are available upon request to Y.J.

643

Acknowledgments

We thank Gilad Haran (Weizmann Institute of Science), Ronen Alon (Weizmann Institute of Science), and Amnon Altman (La Jolla Institute for Immunology) for their kind advice and discussion for the manuscript. This research was supported by Basic Science Research Program through the National Research Foundation of Korea (NRF) funded by the Ministry of Education (2022R1I1A1A01070462) to Y.J.

Author contributions

Y.J. conceived and designed the experiments, Y.K. designed and synthesized the CNPs, Y.J., Y.K, S.L. performed experiments. Y.J. analyzed data, J.N. performed transduction, S.H. performed manual quantification. Y.J. Y.K. and M.K. wrote manuscript, M.K and J. C. co-supervised the project.

Competing interest declaration

The authors declare no competing interests.

Figures

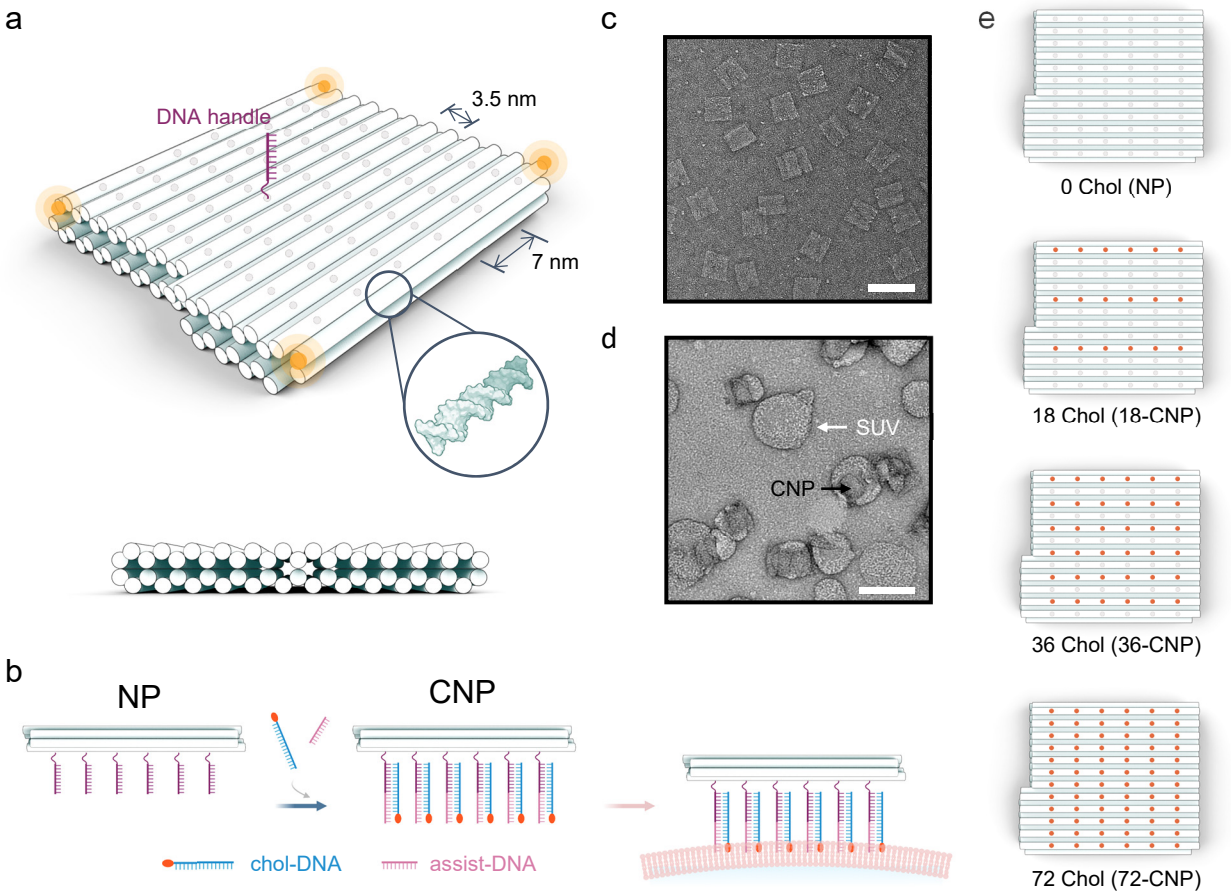

Figure 1. DNA nano-patch (NP) displaying multiple cholesterols. a, A schematic drawing for the DNA-NP structure. Each cylinder represents a double-stranded DNA (dsDNA). Gray circles represent potential locations (anchors) where the DNA handles can be added for binding of Chol-DNAs. Cy5-conjugated ssDNAs were attached at the four corners. The DNA-NP is a square shape of 60 x 60 nm^2 with a 6 nm height. Each anchor is separated by 3.5 and 7 nm in rows and columns, respectively. **b,** Schematic illustration of the construction of cholesterol nano-patch (CNP). Chol-DNAs are complexed to the DNA handles on the DNA NP *via* DNA hybridization. Assist-DNA strands are added together to form a stable duplex form. **c-d,** Representative TEM images of DNA-NP without cholesterols (c) and CNP bound on the surface of small unilamellar vesicles (SUVs) (d). (Scale bars:100 nm). **e,** Schematic illustrations of the spatial arrangement of cholesterol molecules in 18-CNP, 36-CNP or 72-CNP. The positions for the cholesterols are marked with orange dots.

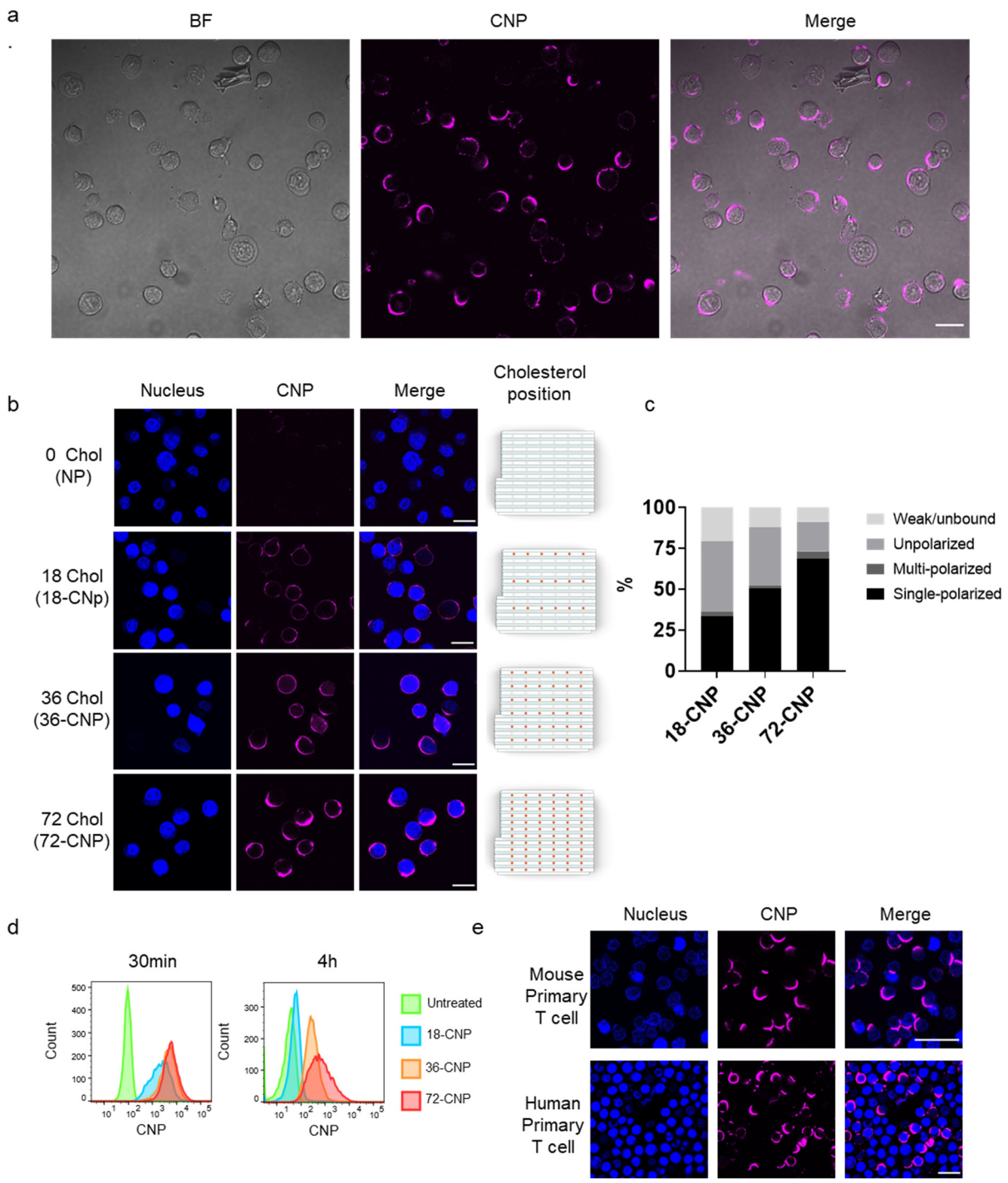

Figure 2. Synthetic lipid rafts on T cell membranes. a, Representative confocal images of Jurkat T cells incubated with 72-CNP for 30 min. Bright-field (BF) (gray, left), 72-CNP (magenta, middle), and the merged images (right) are shown. **b,** Effects of increasing the number of cholesterols on the formation of the synthetic lipid rafts. Representative confocal images of Jurkat T cells incubated with DNA NP without

cholesterol or complexed with 18- (18-CNP), 36- (36-CNP), or 72- (72-CNP) cholesterols for 30 min. Images of nuclei stained with Hoechst (blue, left), CNP (Magenta, middle left), and merged images (middle right) for each sample are presented. The orange dots on the schematic drawings (right) indicate the positions of cholesterols. **c,** The percentage of weak/unbound (light gray), unpolarized (gray), multi-polarized (dark gray), or single-polarized (black) synthetic lipid raft positive cells were counted from Jurkat T cells incubated with 18-(n=120), 36-(n=78), or 72-CNP (n=89) for 30 min (see the **Supplementary Fig. 2d-g**). **d,** Intensity distributions of the different CNPs on single cells incubated for 30 min (left) or 4 h (right) were analyzed by flow cytometry. **e,** Representative confocal images of freshly isolated mouse T cells (upper) or human T cells incubated with 72-CNP for 30 min. (scale bars in a, b and e are 20 μm).

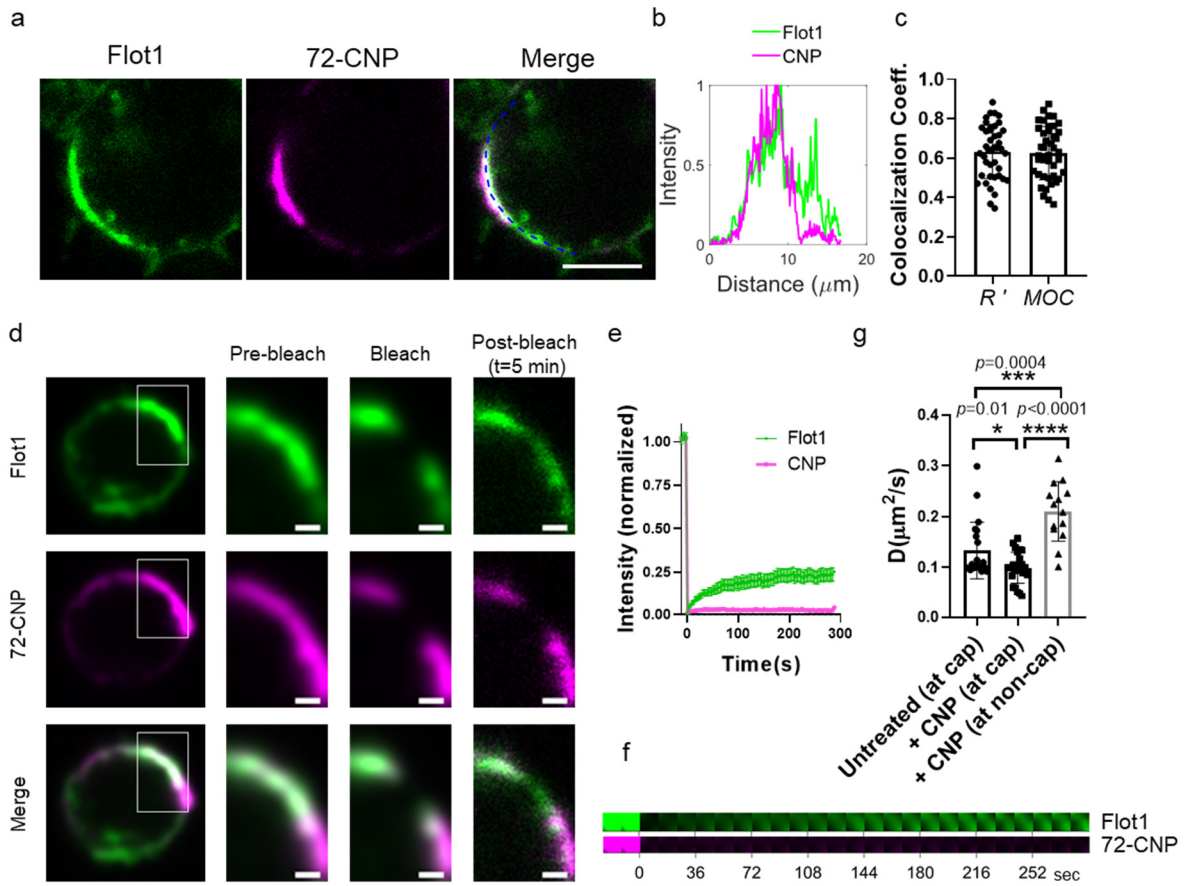

Figure 3. CNP-mediated synthetic lipid rafts colocalized with Flot1-caps. a, Representative confocal images of a Jurkat T cell stably expressing Flot1-Halo incubated with 72-CNP for 30 min. Flot1-Halo labeled with Janelia 549 halotag ligand (green, left), 72-CNP (magenta, middle), and the merged images (right) are presented. **b,** Line profiles of the Flot1 (green) and 72-CNP (magenta) intensities along the blue dashed line in the merged image in **a**. **c,** Quantification of colocalization (Pearson's *R'* and *MOC*) between Flot1 and CNP calculated from 42 cells. Data are mean ± SD. **d-g,** FRAP analysis of the lateral mobility of Flot1 and 72-CNP bound on the membrane. Representative time-lapse confocal images of Flot1 (green) and 72-CNP (magenta) in the area marked by a square in the left images taken before and after bleaching (d). The mean FRAP tracings of Flot1 (green) and 72-CNP (magenta) after photobleaching for 5 minutes from live Jurkat T cells treated with 72-CNP. Data are mean ± SEM (n = 18 cells) (e). The filmstrip showing fluorescence recovery of the bleached area of the cell in **d** marked in **Supplementary Movie 5** (f). The mean diffusion coefficients (D) of Flot1 in untreated (left bar, n= 21) at the cap and in 72-CNP treated cells either at the cap (middle, n=26) or non-cap (right, n=14) areas analyzed from the FRAP (g). Each dot in **c** and **g** represents data collected from a single cell. Error bars are SD. *p*-values (*, $p \leq 0.05$; ***, $p \leq 0.001$, ****, $p \leq 0.0001$) were calculated by two-tailed unpaired t-test. (Scale bars in a and b: 5μm; in e: 1μm).

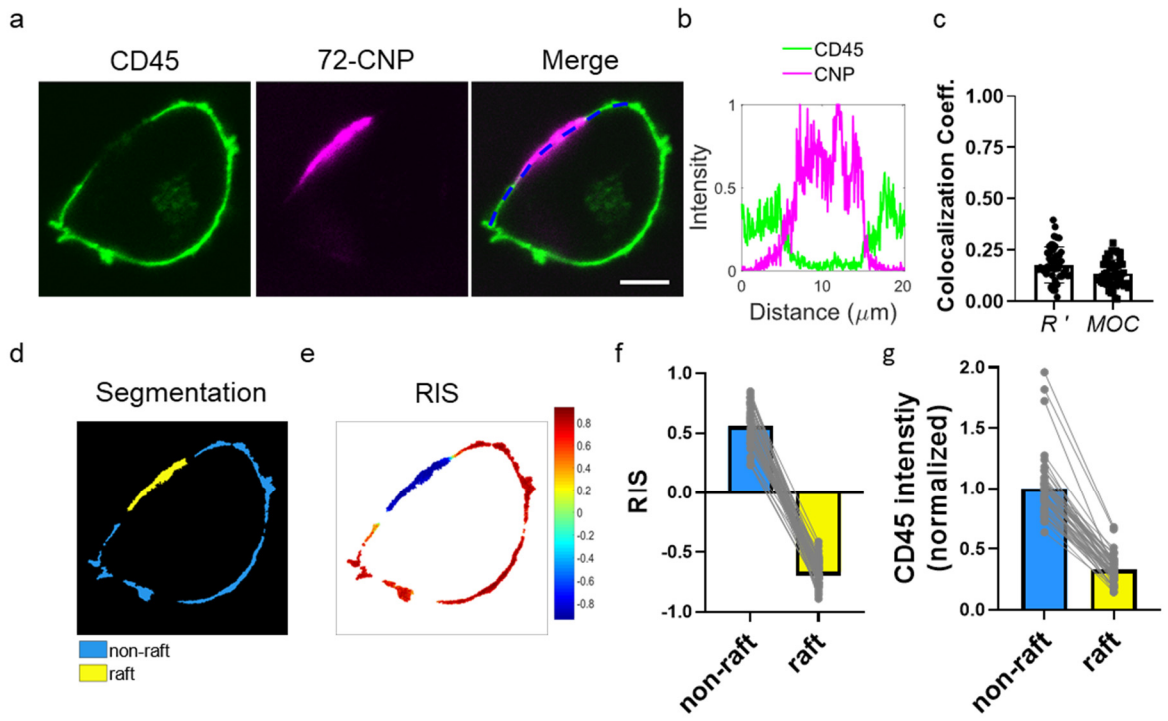

Figure 4. CD45 exclusion mediated by synthetic lipid raft. **a,** Representative confocal images of a Jurkat T cell incubated with 72-CNP for 30 min showing CD45 exclusion from a 72-CNP enriched synthetic lipid raft. CD45 labeled with AF488-conjugated antibody (green, left), 72-CNP (magenta, middle), and the merged images (right) are shown (scale bars: 5μm). **b,** Line profiles of the CD45 (green) and 72-CNP (magenta) intensities along the blue dashed line in **a**. **c,** Quantification of colocalization (Pearson's *R*' and *MOC*) between CD45 and 72-CNP. Each dot represents the data from a single cell (n = 51 cells). Data are mean ± SD. **d,** The segmented map for synthetic lipid raft (raft, yellow) and non-raft (light blue) regions of the cell displayed in **a**. **e,** Ratiometric intensity score (RIS) in each pixel of the entire segmented area presented in d. **f-g,** Paired analysis of the mean RIS values (f) and the mean normalized CD45 intensities (g) of pixels within the segmented areas of the raft vs. non-raft regions. Each grey line represents the data collected from a single cell (n = 51 cells) Data are mean ± SD.

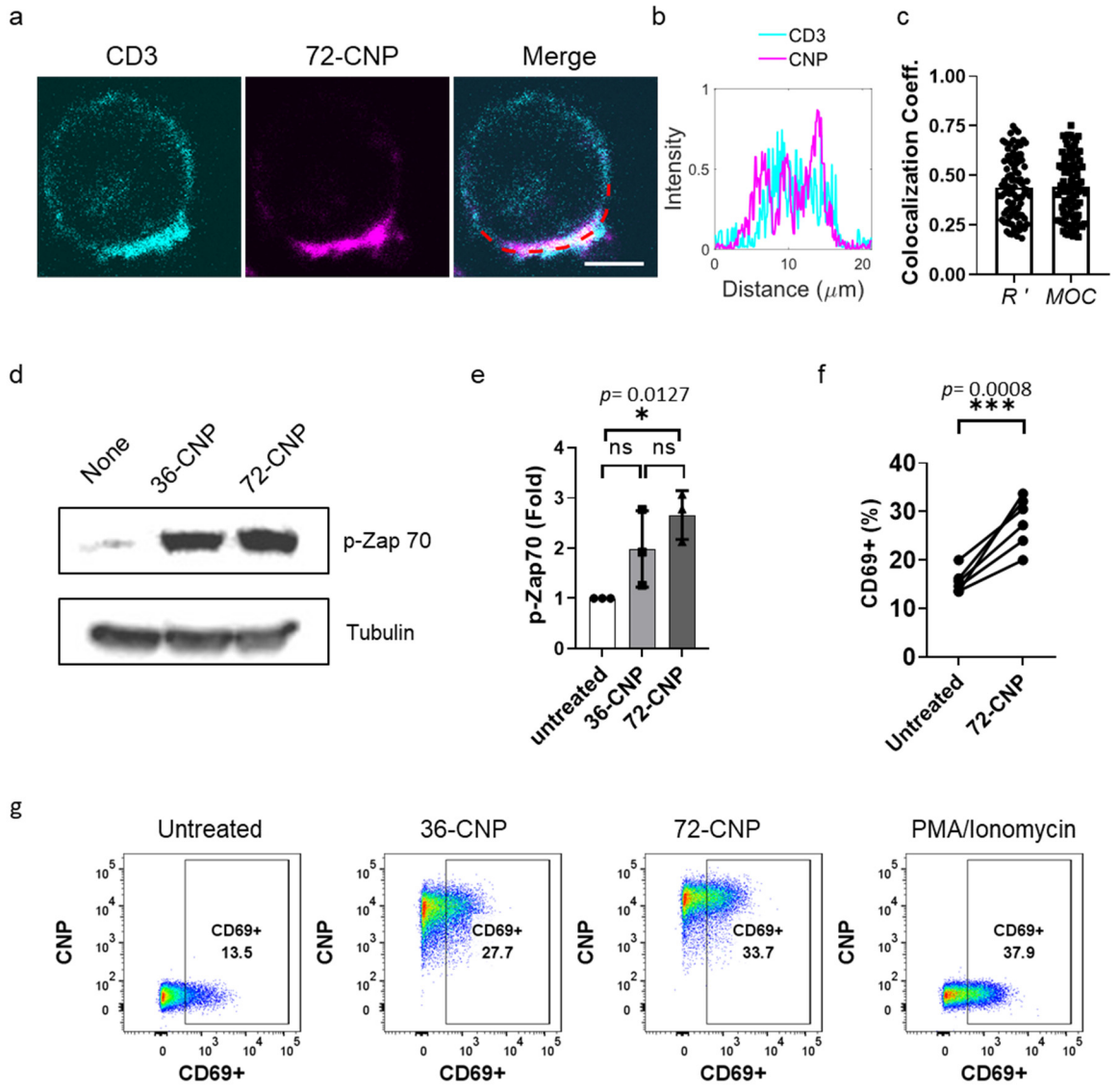

Figure 5. Synthetic lipid rafts activate T cells. a, Representative confocal images of 72-CNP treated Jurkat T cells, showing accumulation of CD3 at 72-CNP induced synthetic lipid rafts. CD3 labeled with AF488-conjugated antibody (cyan, left), 72-CNP (magenta, middle), and the merged images (right) are shown (scale bars: 5μm). **b,** Line profiles of the intensities of the CD3 (cyan) and 72-CNP (magenta) along the red dashed line in the merged image in a. **c,** Quantification of colocalization (Pearson's *R'* and *MOC*) between CD3 and 72-CNP. Each dot represents the data from a single cell (n = 92 cells). Data are mean ± SD. **d-e,** Immunoblot analysis of phosphorylated ZAP-70 (p-ZAP-70) in Jurkat T cells incubated without or with 36- or 72-CNPs for 30 min. Tubulin levels represent the loading control. A representative image of immunoblotting (d) and quantification of p-ZAP-70 levels (e). The intensity of each p-ZAP-70 band relative

to respective tubulin or β-actin band was normalized to that of untreated samples. Each dot represents the band intensity quantified from an individual immunoblotting experiment. Data are mean ± SD. **f-g,** Flow cytometry analysis of CD69 expression induced by CNP. The increments of CD69+ population of cells in 72-CNP treated cells compared to untreated cells obtained from 6 independent experiments (f). A representative set of CD69+ cells in untreated, 36- or 72-CNPs, or in PMA and Ionomycin treated cells gated in a square for each (g). In **e** and **f**, *p*-values (*, $p \leq 0.05$; ***, $p \leq 0.001$) were calculated by the two-tailed ratio paired t-test.

656